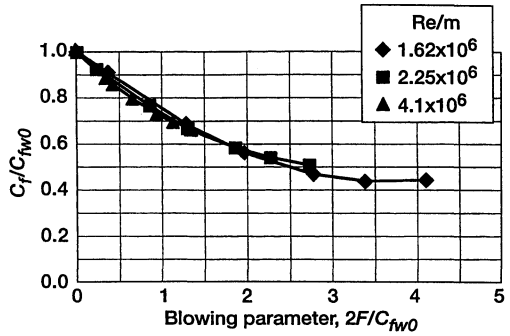

Fig. 3 Skin-friction ratio (based on C_{fw0}) of NASA PN2 as a function of blowing parameter.

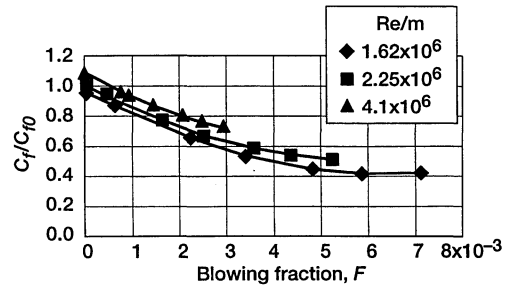

Fig. 4 Skin-friction ratio (based on C_{f0}) of NASA PN2 as a function of blowing fraction.

more than a solid flat-plate value. These plates were regarded as MBT skins. The unblown skin-friction ratios were so high for the other skins that reducing them to below a solid flat-plate value was not possible for practical application. Notice that the holes in the MBT skins have aspect ratios of 4 or higher (Table 1). These small, high-aspect-ratio holes not only are able to control the vertical blowing air during the microblowing but also are able to provide low skin friction without blowing. It also is believed that the slip flow on the surface of the MBT skin plays an important role in reducing the skin friction. The results of PN2 are presented herein.

In Fig. 3 the traditional parameters for injection are used to show the results for NASA PN2 porous plates. As expected, the data collapsed. However, because the collapsed data depend highly on the characteristics of the porous plate, no attempt has been made to compare them with the existing data. Because the skin-friction ratio C_{fw0}/C_{f0} is so different for various unblown porous plates (see Fig. 2), Fig. 3 provides only limited information about the effectiveness of a porous plate for blowing boundary-layer control. A more meaningful way to present the data for the NASA PN2 porous plates is shown in Fig. 4. Note that the reference skin-friction coefficient is that of a flat plate, C_{f0} instead of C_{fw0}.

Figure 4 indicates that, for PN2, even an extremely small amount of blowing air, i.e., $F < 0.0005$, reduced the skin friction below that of the solid flat plate and continued to reduce it effectively at a blowing fraction $F < 0.003$ with higher rate of skin-friction reduction. This small amount of blowing air is called the microblowing. The penalty for supplying blowing air in the MBT is probably very low because the blowing flow rate is so small. Figure 4 shows that up to 60% reduction ($C_f/C_{f0} = 0.4$) was achieved for this porous plate. A smaller reduction below the flat-plate value was shown at higher Reynolds numbers, as can be seen in Fig. 4 for the NASA PN2 porous plate.

Concluding Remarks

A proof-of-concept experiment (phase I) for the Micro-Blowing Technique (MBT) has been successfully completed. Preliminary results show that, with microblowing, up to 60% skin-friction reduction below a flat-plate value can be achieved over a wide range of flow conditions. Research indicates that the skin is the most important factor in achieving success with the MBT. This experiment identified three skins for use with the MBT, all having holes with aspect ratios larger than 4. One of the ways that the MBT reduces skin friction is by effectively reducing the roughness of the skin by means of very low blowing air. More experiments are required to determine the optimal MBT skin and to assess the penalty associated with this technique.

References

[1]Bushnell, D. M., and Hefner, J. N., *Viscous Drag Reduction in Boundary Layers*, Vol. 123, Progress in Astronautics and Aeronautics, AIAA, Washington, DC, 1990.

[2]"Special Course on Skin Friction Drag Reduction," AGARD R-786, 1992.

[3]Wilkinson, S. P., "Influence of Wall Permeability on Turbulent Boundary-Layer Properties," AIAA Paper 83-0294, Jan. 1983.

[4]Beltran, L. R., Del Roso, R. L., and Del Rosario, R., "Advanced Nozzle and Engine Components Test Facility," NASA TM-103684, 1992.

[5]Hwang, D. P., "A Proof-of-Concept Experiment for Reducing Skin Friction by Using a Micro-Blowing Technique," AIAA Paper 97-0546, Jan. 1997.

A. Plotkin
Associate Editor

Hybrid Turbulence Model for Unsteady Boundary Layers

David Greenblatt*
Tel Aviv University, Ramat Aviv 69978, Israel

Introduction

DURING the 1990s dynamic stall has remained an area of active research, primarily due to its occurrence in important applications such as high-angle-of-attack aerodynamics, rapidly maneuvering aircraft, helicopter rotors, wind turbines, and turbomachinery. The application of viscous–inviscid interaction methods[1] or Navier–Stokes solvers,[2] combined with turbulence models of varying complexity, to oscillating airfoils and wings has become prevalent in the last few years. A spectrum of models ranging from algebraic to two-equation models has been employed, and their results have been compared with airfoil integrated-load data ranging from attached flow through airfoil flutter (light stall) to massively separated flow (deep stall). By and large, the results are unsatisfactory, with attached and massively separated flow modeling attaining the best predictions, whereas light stall predictions are somewhat inferior.[3] For example, recent airfoil flutter investigations[2,4] revealed that a variety of turbulence models were unable to predict the pitching moment history, which is crucial for predicting rotor life.

There are many factors that influence the accuracy of current computational schemes. Carr and McCroskey[3] have identified turbulence modeling, grid dependencies, artificial viscosity, and the choice of numerical scheme as important areas that need to be addressed if computational efforts are to be directly useful. Ekaterinaris and Menter[2] have demonstrated the importance of transition modeling to capture the dynamic stall physical mechanisms. This study was undertaken to avoid the problem areas associated with both numerical artifacts, limiting boundary-layer assumptions, as well as physically ambiguous phenomena such as transition modeling, and unknown upstream influences. Here, the emphasis was placed on developing an unsteady turbulence model and then testing the model, per se, by comparing it to definitive experimental data. Consequently, this preliminary investigation considered a streamwise fully developed, large-amplitude pulsating turbulent pipe flow near separation rather than an unsteady boundary layer or a dynamic stall scenario, thus minimizing the aforementioned problems. The principal common denominators are that both flows are subjected to large, time-dependent streamwise pressure gradients and that both

Received Aug. 5, 1997; revision received Nov. 9, 1997; accepted for publication Nov. 21, 1997.

*Junior Faculty Member, Department of Fluid Mechanics and Heat Transfer, Faculty of Engineering.

have similar structure in the near-wall region. The fully developed pipe flow momentum equation is a parabolic Navier–Stokes problem and, thus, avoids boundary-layer-type assumptions and can be solved by robust numerical methods. In addition, because the problem is one dimensional in space, upstream influences are eliminated, an extremely fine grid can be employed in the near-wall region without excessive computational cost, and artificial viscosity is not significant.

In this Note, a hybrid model is developed and evaluated for a single data set. For a broader perspective, the results of algebraic, one-equation,[5] and two-equation[6] models are also presented. The algebraic model was composed of the van Driest near-wall mixing length with the Cebeci–Keller[7] unsteady modification and the Cebeci–Smith[8] outer-layer eddy viscosity. The one-equation[5] model was based on the Norris–Reynolds[9] Prandtl-energy model with a prescribed mixing length. The two-equation[6] model was based on that of Jones and Launder,[10] making use of wall functions for computational efficiency.

Model Composition

The model developed here is termed a hybrid model because it blends two independently developed concepts into a single model. The first component is based on the ideas expressed by Mao and Hanratty[11] (MH), which accounts for the unsteady effects in the viscous sublayer, whereas the second component is based on the popular Johnson–King[12] (JK) turbulence model. The MH model was considered as an important component of this model due to its ability to predict unsteady viscous sublayer phenomena, an issue not explicitly addressed in current unsteady models. The JK model was selected due to its relatively good static and dynamic performance,[13,14] low computational cost, and ease of implementation.

Viscous-Region Relaxation Model

Based on the observation that steady favorable and unfavorable pressure gradients, respectively, dampen and enhance near-wall turbulence, a number of investigators, e.g., Launder and Jones,[15] have argued that this behavior increases or decreases the viscous sublayer thickness. This is typically represented by allowing the constant A^+ to be a function of the dimensionless pressure gradient $p^+ = (\mathrm{d}p/\mathrm{d}x)\nu/\rho u_\tau^3$ in the following manner:

$$A^+ = A_0^+\left(1 + k_1 p^+ + k_2 p^{+2} + \cdots\right) \tag{1}$$

where A_0^+ and $k_1, k_2, \ldots$, are constants (15 and $-40, 0$, respectively).

In situations where the steady pressure gradient varies rapidly is the streamwise direction, first-order lag equations have been proposed, e.g., Ref. 15. Mao and Hanratty[11] have extended this idea to small-amplitude unsteady flows, and the effective pressure gradient is described by

$$\frac{\mathrm{d}p_{\mathrm{eff}}^+}{\mathrm{d}t^+} = \frac{p^+ - p_{\mathrm{eff}}^+}{k_L} \tag{2}$$

where k_L is a relaxation constant (220). The effect of this model is ultimately included in the van Driest damping term: $D = 1 - \exp(-yu_\tau/\nu A^+)$.

Unsteady JK Model

Development of the unsteady half-equation form of the model presented next closely follows the general arguments of Johnson and King.[12] Minor modifications have been implemented here to render the model applicable to pipe flow geometry, and extension of the unsteady version to boundary layers is straightforward. The JK model incorporates both equilibrium and nonequilibrium modeling ideas. The equilibrium eddy viscosity distribution can be expressed as

$$\nu_{ti,\mathrm{eq}} = D^2\kappa y\langle -u'v'\rangle_{m,\mathrm{eq}}^{\frac{1}{2}} \tag{3a}$$

$$\nu_{to,\mathrm{eq}} = \alpha a u_\tau \tag{3b}$$

$$\nu_{t,\mathrm{eq}} = \nu_{to,\mathrm{eq}}\left[1 - \exp(-\nu_{ti,\mathrm{eq}}/\nu_{to,\mathrm{eq}})\right] \tag{3c}$$

where κ is the von Kármán constant (0.4), α is an outer-layer constant (0.08), and a is the pipe radius.

In similar fashion to the relationship introduced earlier, the nonequilibrium inner-layer eddy viscosity is given by $\nu_{ti} = D^2\kappa y\langle -u'v'\rangle_m^{1/2}$, whereas that in the outer layer is determined by satisfying the relationship $\nu_{t,m} = \langle -u'v'\rangle_m(\partial u/\partial y)_m$ with $\nu_t = \nu_{to}[1 - \exp(-\nu_{ti}/\nu_{to})]$.

To utilize this model, an equation is required for the velocity scale $\langle -u'v'\rangle_m^{1/2}$. This is achieved by considering the ensemble-averaged turbulent kinetic energy equation for the region outside of the viscous sublayer at the time-dependent point of maximum kinetic energy, with the assumptions $\varepsilon_m = k_m^{3/2}/L_m$ and $\langle -u'v'\rangle_m = a_1 k_m$ and with diffusion modeling based on Townsend's bulk convection hypothesis resulting in

$$\frac{\mathrm{d}g}{\mathrm{d}t} = \frac{a_1}{2L_m}\left(1 - \frac{g}{g_{\mathrm{eq}}}\right) + \frac{C_{\mathrm{dif}}}{2}\Phi_m \tag{4}$$

The constants a_1 and C_{dif} took on values appropriate to pipe flow geometry (0.1 and 0.65, respectively). The diffusion modeling employed by Johnson and King[12] could not be justified in the context of a pipe flow geometry and, consequently, $\Phi_m = 1$. For the pipe flow dissipation length scale, the standard Nikuradse formula was used.[16]

Numerical Solution

The pipe flow momentum equation is solved by means of a second-order accurate finite difference numerical scheme similar to that of Mao and Hanratty.[11] The computational grid was graded, with a larger relative grid density in the near-wall region. A total of 120 cross-stream grid points were used, and it was ascertained that halving this number brought about negligible changes to the computed results. The method was validated against classical solutions for pulsating and transient laminar flow problems resulting in accuracies of $\mathcal{O}(0.1)\%$. The code was further validated for steady turbulent flows and accurately predicted the laminar sublayer, log-law region, and wake region. The first grid point was positioned at $y^+ = 0.2$, and 16 grid points were located in the region $y^+ < 5$. This excessive grid density was justified because the constant A^+ varied from 15 to ~1 during flow deceleration, indicating excessive thinning of the sublayer region. The JK equation for g [Eq. (4)] was solved, simultaneously, by a fourth-order Runge–Kutta method.

Results and Discussion

The computed results were validated against the definitive incompressible experimental data of Ramaprian and Tu,[17] where the cross-section instantaneous velocity varied as $U = \bar{U} + \tilde{U}\exp(i\omega t)$, with Reynolds number $\bar{U}2a/\nu = 50{,}000$, dimensionless frequency $\omega a/\bar{U} = 0.08$, and oscillation amplitude $\tilde{U}/\bar{U} = 0.65$. Velocity profile measurements $u = \bar{u}(r) + \tilde{u}(r)\exp i[\omega t - \phi(r)]$ were made with a laser Doppler velocimeter, and the wall shear stress was measured by means of flush-mounted hot-film probes. The oscillations were achieved computationally by subjecting the steady flow turbulent profile to an unsteady sinusoidal pressure gradient corresponding to the appropriate nondimensional amplitude and frequency. The solution was considered to be converged when there was negligible difference between successive cycles.

Normalized velocity profile amplitudes for the experimental data, as well as the results of the four turbulence models, are presented in Fig. 1. Apart from the hybrid model proposed here, all models exhibit deficiencies across virtually the entire pipe radius. For the region close to the wall, $r/a > 0.75$, both the algebraic and the k–ε models overpredict the data, whereas the k model overpredicts in the region very close to the wall and then begins to underpredict the data as the core region of the pipe is approached. For the core region of the pipe, the situation is reversed. On the other hand, the hybrid model predicts the trend significantly better than the other models with small, alternating under- and overpredictions. The small deviations can probably be attributed to relative simplicity of the models, which are both essentially first-order history effects for the eddy viscosity velocity and length scales. It is important to note that the JK model, when employed without the MH viscous sublayer modification, fails

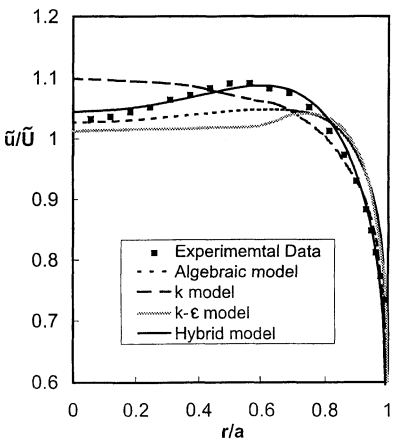

Fig. 1 Amplitude profile comparison with data.

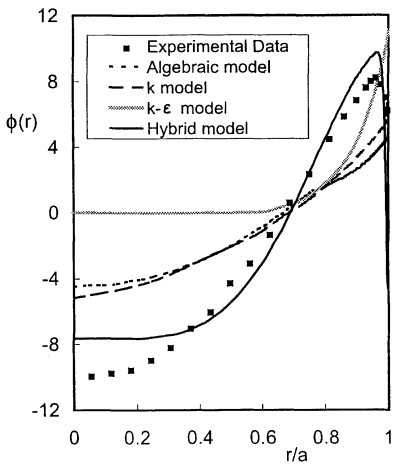

Fig. 2 Phase-shift profile comparison with data.

to predict the data trend in both near-wall and core regions. This intriguing observation is discussed later.

Figure 2 shows the phase shift associated with the amplitude profiles of Fig. 1. All models, apart from the hybrid model, exhibit large deviations from the data. These models capture neither the phase-lead maximum in the near-wall region nor the relatively large phase lag in the core region. The k–ε model yields slightly superior predictions in the near-wall region but inferior predictions in the core region, whereas the opposite is true for the algebraic and k models. The phase-shift prediction of the hybrid model is far superior to the other models. The location of the phase-lead maximum is well predicted but is too large by approximately $1\frac{1}{2}$ deg. The hybrid model prediction is also superior in the core region, overpredicting the phase lag by about 2 deg. The relatively small overpredictions of the phase shift associated with the hybrid model are attributed, as earlier, to the relative simplicity of both model components.

The results presented in Figs. 1 and 2 illustrate the important result that an unsteady turbulence model is only as strong as its weakest element. To illustrate this, consider the normalized statement of mass conservation for the oscillating velocity component in the pipe, viz.,

$$\frac{2}{a^2\tilde{U}}\int_0^a r\tilde{u}(r)\exp[-i\phi(r)]\,\mathrm{d}r = 1 \tag{5}$$

If $\phi(r)$ is small across the extent of the pipe, which is the case here, an amplitude overprediction in the near-wall region must be balanced by an underprediction in the core region, and vice versa, to satisfy mass conservation. With larger phase shifts, the problem is compounded, because both amplitude and phase errors must be balanced. Therefore, failure to adequately model the viscous sublayer, particularly when the boundary layer is subjected to large unsteady pressure gradients, can have detrimental effects on the predictions across the extent of the boundary layer. The same is true in the outer layer, where setting $C_{\mathrm{dif}} = 0$ had a similar impact.

Skin-friction history (as a function of angle ωt) comparisons for all turbulence models are presented in Fig. 3. In keeping with both

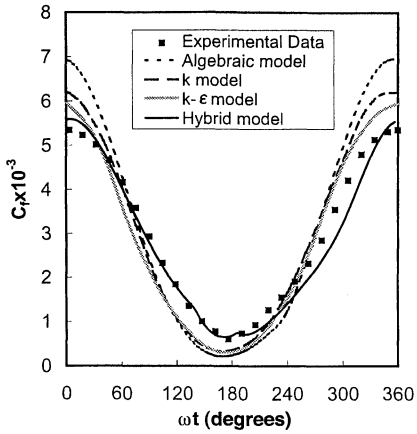

Fig. 3 Skin-friction history comparison with data.

sets of earlier results, all models with the exception of the hybrid model significantly over- and underpredict the skin-friction maxima and minima, respectively. All of these models also fail to predict the skin-friction history at any stage during cycle. The hybrid model, however, slightly overpredicts the maximum, closely follows the data during the deceleration, accurately predicts the minimum, and then somewhat underpredicts the upstroke data. The reason for the discrepancy in the upstroke data was that too much viscous sublayer thickening was predicted by the simple linear model employed here. Whereas the constant $k_1 = -40$ was appropriate for the adverse pressure gradient, as can be seen by the downstroke comparison, this constant was too large for the favorable pressure gradient. For steady flows with streamwise pressure gradients it is common to use a nonlinear model for the viscous sublayer.[18] For the results presented here, however, no attempt was made to optimize the hybrid model in any way because the small-amplitude linear unsteady model of Mao and Hanratty was used directly.

Concluding Remark

Although this model is capable of satisfactory near-wall predictions near separation, the MH dependence on u_τ presents a problem when extending the current model to unsteady separating flows. Moreover, the lack of reliable near-wall measurements of unsteady separating turbulent boundary layers further complicates modeling this region. Consequently, for extensions of the MH model component to regions of separating flow, two approaches are suggested. The first is to replace u_τ with $|u_\tau|$ and the physical requirement that $A^+ \geq 0$ (e.g., Ref. 18). Alternatively, the velocity scale u_τ may be replaced by $\langle -u'v'\rangle_m^{1/2}$, which is consistent with the JK model component and does not materially change the attached flow results.

References

[1]Carr, L. W., Platzer, M. F., Chandrasekaha, M. S., and Ekaterinaris, J., "Experimental and Computational Studies of Dynamic Stall," *Numerical and Physical Aspects of Aerodynamic Flows IV*, edited by T. Cebeci, Springer–Verlag, Berlin, 1990, pp. 239–256.

[2]Ekaterinaris, J. A., and Menter, F. R., "Computation of Oscillating Airfoil Flows with One- and Two-Equation Turbulence Models," *AIAA Journal*, Vol. 32, No. 12, 1994, pp. 2359–2365.

[3]Carr, L. W., and McCroskey, W. J., "A Review of Recent Advances in Computational and Experimental Analysis of Dynamic Stall," *IUTAM Symposium on Fluid Mechanics of High Angle of Attack* (Tokyo, Japan), International Union of Theoretical and Applied Mechanics, 1992, pp. 1–22.

[4]Ko, S., and McCroskey, W. J., "Computations of Unsteady Separating Flows over an Oscillating Airfoil," *AIAA Journal*, Vol. 35, No. 7, 1997, pp. 1235–1238.

[5]Ramaprian, B. R., and Tu, S. W., "Study of Periodic Turbulent Pipe Flow," Iowa Inst. of Hydraulic Research, Rept. 238, 1982.

[6]Mankbadi, R. R., "Fully Developed Pulsating Turbulent Flows," *AIAA/ASME/SIAM/APS 1st National Fluid Dynamics Congress* (Cincinnati, OH), AIAA, Washington, DC, 1988, pp. 376–383.

[7]Cebeci, T., and Keller, H. B., "On the Computation of Unsteady Turbulent Boundary Layers," *Recent Research on Unsteady Boundary Layers*, edited by E. A. Eichelbrenner, 1972, pp. 1072–1105.

[8]Cebeci, T., and Smith, A. M. O., *Analysis of Turbulent Boundary Layers*, Academic, New York, 1974, pp. 111, 112.
[9]Norris, H. L., and Reynolds, W. C., "Turbulent Channel Flow with a Moving Wavy Boundary," Mechanical Engineering Dept., Rept. TF-7, Stanford Univ., Stanford, CA, 1975.
[10]Jones, W. P., and Launder, B. E., "The Prediction of Laminarization with a Two-Equation Model of Turbulence," *International Journal of Heat and Mass Transfer*, Vol. 15, 1972, pp. 301–314.
[11]Mao, Z.-X., and Hanratty, T. J., "Studies of the Wall Shear Stress in a Turbulent Pulsating Pipe Flow," *Journal of Fluid Mechanics*, Vol. 170, 1986, pp. 545–564.
[12]Johnson, D. A., and King, L. S., "A Mathematically Simple Turbulence Closure Model for Attached and Separated Turbulent Boundary Layers," *AIAA Journal*, Vol. 23, No. 11, 1985, pp. 1684–1692.
[13]Clarkson, J. D., Ekaterinaris, J. A., and Platzer, M. F., "Computational Investigation of Airfoil Stall Flutter," *Unsteady Aerodynamics, Aeroacoustics and Aeroelasticity of Turbomachines and Propellers*, edited by H. M. Atassi, Springer–Verlag, 1991, pp. 415–432.
[14]Menter, F. R., "Performance of Popular Turbulence Models for Attached and Separated Adverse Pressure Gradient Flows," *AIAA Journal*, Vol. 30, No. 8, 1992, pp. 2066–2072.
[15]Launder, B. E., and Jones, W. P., "Sink Flow Turbulent Boundary Layers," *Journal of Fluid Mechanics*, Vol. 38, Pt. 4, 1969, pp. 817–831.
[16]Schlichting, H., *Boundary Layer Theory*, McGraw–Hill, New York, 1979, pp. 604, 605.
[17]Ramaprian, B. R., and Tu, S. W., "Fully Developed Periodic Turbulent Pipe Flow. Part 2. The Detailed Structure of the Flow," *Journal of Fluid Mechanics*, Vol. 137, 1983, pp. 59–81.
[18]Crawford, M. E., and Kays, W. M., "STAN5—A Program for Numerical Computation of Two-Dimensional Internal and External Boundary Layer Flows," NASA-CR 2742, 1976.

C. G. Speziale
Associate Editor

Reordering of Hybrid Unstructured Grids for Lower–Upper Symmetric Gauss–Seidel Computations

Dmitri Sharov* and Kazuhiro Nakahashi†
Tohoku University, Sendai 980-77, Japan

I. Introduction

THE advantages of an unstructured grid over a structured grid are lower cost of grid generation, adaptive refinement/unrefinement capabilities, and savings in total number of grid points. However, most unstructured grid computations are computationally very expensive, especially for high Reynolds number flows, because conventional implicit time-integration methods based on grid line sweeps for structured grids are not suitable for unstructured grids.

Recently the lower–upper symmetric Gauss–Seidel (LU-SGS) approximate factorization,[1] which is very efficient for structured grids, has been implemented to unstructured grids by several authors.[2–4] Those methods do not require extra storage, are free from any matrix inversion, and demonstrate performance similar to the structured grid schemes.

This Note is devoted to the three-dimensional hybrid grid implementation of the LU-SGS method proposed in Ref. 2. The original method was based on sweeps through grid node numbers and was applied to two-dimensional Euler computations. Unfortunately, in its original formulation, the method cannot be vectorized; in addition the method is not compatible with commonly used edge-based data structure. To fit the method to the three-dimensional computations on a vector supercomputer, grid reordering is necessary. In Ref. 3, such a reordering was proposed. However, it was applied to the cell-centered finite volume method, and the LU-SGS formulation was different from that of Ref. 2.

Here a grid reordering method for a cell-vertex scheme on hybrid grids is proposed. This reordering provides good convergence properties, as well as vectorization capability of the code. The method has been tested on several three-dimensional tetrahedral as well as hybrid (prismatic/pyramidal/tetrahedral) grids. The Euler and Navier–Stokes equations have been computed.

Received March 10, 1997; presented as Paper 97-2102 at the 13th Computational Fluid Dynamics Conference, Snowmass Village, CO, June 29–July 2, 1997; revision received Aug. 5, 1997; accepted for publication Nov. 17, 1997.

*Assistant Professor, Department of Aeronautics and Space Engineering; currently Researcher, Research Center for Computational Science, Fujitsu, Ltd., 9-3, Nakase 1-chome, Mihama-ku, Chiba-shi 261, Japan. Member AIAA.
†Professor, Department of Aeronautics and Space Engineering. Associate Fellow AIAA.

II. Finite Volume Discretization

The governing Navier–Stokes equations are solved by the finite volume cell-vertex scheme. The control volumes are nonoverlapping dual cells constructed around each node i. Each edge connecting two nodes i and j is associated with vector area $\boldsymbol{s}_{ij}$, and gas dynamic fluxes are computed through the areas $\boldsymbol{s}_{ij}$. To enhance the accuracy of the scheme, a linear reconstruction of the primitive gas dynamic variables inside the control volume is used. Venkatakrishnan's limiter[5] is used because of its superior convergence properties. After the reconstruction, a flux quadrature is performed around each control volume using a single point along each face of the control volume. The flux is computed using a Harten–Lax–van Leer–Einfeldt–Wada approximate Riemann solver.[6]

To compute viscous stress and heat flux terms it is necessary to evaluate spatial derivatives of the primitive variables at each control volume face. These spatial derivatives are evaluated directly at the edges. The derivatives are computed by looping once through all grid cells and accumulating the result at the grid edges.

III. LU-SGS Method for Unstructured Grids

The LU-SGS formulation[2] can be described as follows.
Forward sweep:

$$\Delta \boldsymbol{Q}_i^* = \boldsymbol{D}^{-1}\left[\boldsymbol{Res}_i - 0.5\sum_{j:j\in L(i)}\left(\boldsymbol{s}_{ij}\cdot\Delta\boldsymbol{F}_j^* - |\boldsymbol{s}_{ij}|\rho_{A_j}\Delta\boldsymbol{Q}_j^*\right)\right] \quad (1a)$$

Backward sweep:

$$\Delta \boldsymbol{Q}_i = \Delta\boldsymbol{Q}_i^* - 0.5\boldsymbol{D}^{-1}\sum_{j:j\in U(i)}\left(\boldsymbol{s}_{ij}\cdot\Delta\boldsymbol{F}_j - |\boldsymbol{s}_{ij}|\rho_{A_j}\Delta\boldsymbol{Q}_j\right) \quad (1b)$$

where

$$\boldsymbol{D} = \left(\frac{\mathrm{Vol}_i}{\Delta t} + 0.5\sum_{j(i)}\rho_{A_i}|\boldsymbol{s}_{ij}|\right)\boldsymbol{I}$$

and

$$\boldsymbol{Res}_i = -\sum_{j(i)}\boldsymbol{s}_{ij}\cdot\boldsymbol{F}_{ij} + \sum_{j(i)}\boldsymbol{s}_{ij}\cdot\boldsymbol{R}_{ij}$$

where $\boldsymbol{Q}$ is the state vector; $\boldsymbol{F}$ comprises the convective flux vector components $\boldsymbol{F}_x$, $\boldsymbol{F}_y$, and $\boldsymbol{F}_z$; and $\boldsymbol{R}$ is the viscous flux vector components $\boldsymbol{R}_x$, $\boldsymbol{R}_y$, and $\boldsymbol{R}_z$. $\boldsymbol{Res}_i$ is the explicit quadrature of convective fluxes and viscous stresses, and ρ_A is the spectral radius of the Jacobian matrix $\boldsymbol{A} = \delta\boldsymbol{F}/\delta\boldsymbol{Q}$. For stable viscous computations the local diffusion velocity $v/\Delta x$ must be added to the spectral radius.

The method requires no special treatment of boundaries. Contributions from boundary faces must be considered only for the computation of the diagonal matrix $\boldsymbol{D}$.

The important issue for the unstructured grid LU-SGS methodology is the determination of lower and upper matrices; that is, how to determine the sets $L(i)$ and $U(i)$ in Eq. (1). The next section discusses this issue.